

High-resolution deep view microscopy of cells and tissues

H. Schneckenburger, V. Richter, M. Gelleri, S. Ritz, R. Vaz Pandolfo, F. Schock, J. v. Hase, U. Birk, C. Cremer

Abstract. Methods, experimental setups and perspectives of three-dimensional deep view imaging microscopy of cell or tissue samples are reported. Preliminary biophysical and clinically relevant examples are presented.

Keywords: 3D microscopy, fluorescence, super-resolution, SIM, light sheet, axial tomography, distributed apertures.

1. Introduction

Optical microscopy is a well-established method with excellent perspectives for live cell experiments, but also with some limitations concerning resolution, depth of focus and light scattering. Resolution d_{\min} is well described by the Abbe or the Rayleigh criterion. While the Abbe criterion $d_{\min} \geq \lambda/2A_N$ (with λ is the wavelength of light and A_N is the numerical aperture of the microscope objective lens) results from diffraction of a coherent light beam, the Rayleigh criterion $d_{\min} = 0.61\lambda/A_N$ results from the diffraction function of an incoherently luminescent spot (Airy disk). In both cases, lateral resolution values around 200 nm are attained for high numerical apertures ($A_N \geq 1.30$) and around 400–500 nm for moderate apertures ($A_N \leq 0.60$), e.g. upon imaging of larger objects with long-distance objective lenses.

Optical microscopy inside a medium with a refractive index n provides a depth of focus $L = n\lambda/A_N^2$, which is in the range of about 400 nm up to several micrometers. For low numerical apertures required to realise large working distances (WDs), the focal depth may increase to the multi-micrometer range (e.g. $L = 91 \mu\text{m}$ for $A_N = 0.1$, $\lambda = 600 \text{ nm}$, and $n = 1.515$). Irrespective of the numerical aperture, the decay of the detected intensity from outside the focal plane is insuffi-

cient to warrant discrimination of multiple stacked object layers. This implies that only from thin layers sharp images can be generated, and that special techniques are needed for imaging three-dimensional (3D) samples. 3D resolution has been introduced by confocal laser scanning microscopy (CLSM), where the focus of a laser beam scanning the sample is imaged on a pinhole in front of the detector, while all out-of-focus information is suppressed [1, 2]. By moving the sample step by step in a vertical direction, images of numerous planes can thus be recorded and combined in a 3D image. Alternatively, samples are illuminated by a thin light sheet that is in the focus of the detection lens (light-sheet based microscopy, LSFM). Such light sheets are generated either by a cylindrical lens, by scanning a laser beam, or more generally by adaptive beam shaping devices [3, 4]. The 3D image is acquired by either moving the light sheet in the vertical direction with a simultaneous shift of the detection lens, or (in some cases) by moving the sample through the image plane. In contrast to CLSM only the thin object layer from which signal is detected has to be exposed to light, so that the total light exposure in 3D imaging is considerably lower. This favors LSFM for experiments performed over a long time range. Experimental setups for the LSFM range from stand-alone microscopes to miniaturised modules, which can be adapted to various kinds of commercial microscopes and combined with further experimental techniques [5, 6].

A major problem for imaging deeper layers of a cell assembly or a tissue sample is light scattering (and to a lower extent also absorption) limiting penetration depths to typically 100 μm or less. For this reason optical clearing techniques matching the refractive indices of a tissue and a surrounding medium have gained considerable importance for deep view imaging of skin, brain and other organs [7–9]. However, optical clearing techniques are not compatible with live cell imaging, and for this reason, alternative methods of optical microscopy are needed.

2. Methods and applications of 3D deep view microscopy

2.1. Confocal Microscopy

Confocal microscopy has been further developed in recent years. In particular, Airy scan microscopy [10] and the related image scanning microscopy [11] as well as re-scanning confocal microscopy [12] made it possible to improve resolution by about a factor of 1.7. Long-wavelength (red or near-IR) light with lower scattering and absorption coefficients permits imaging 2–3 times deeper inside tissue (i.e. up to 200–300 μm). This holds in particular for two-photon or multi-photon

H. Schneckenburger, V. Richter Institute of Applied Research, Aalen University, Aalen, Germany;

e-mail: herbert.schneckenburger@hs-aalen.de;

M. Gelleri, S. Ritz Institute of Molecular Biology, Mainz, Germany;

R. Vaz Pandolfo Institute of Molecular Biology, Mainz, Germany; Institute of Physiology, University Medical Center of the Johannes Gutenberg University, Mainz, Germany;

F. Schock, J. von Hase Kirchhoff Institute for Physics (KIP), and Institute of Pharmacy & Molecular Biotechnology, University of Heidelberg, Germany;

U. Birk Institute for Photonics and ICT, University of Applied Sciences (FHGR) Chur, Switzerland;

C. Cremer Institute of Molecular Biology, Mainz, Germany; Kirchhoff Institute for Physics (KIP), and Institute of Pharmacy & Molecular Biotechnology, University of Heidelberg, Germany

Received 27 November 2019

Kvantovaya Elektronika 50 (1) 2–8 (2020)

Submitted in English

microscopy [13, 14]. Here, picosecond or femtosecond laser pulses are focused onto a small spot permitting fluorescence to be detected exclusively from this spot. Different planes of a specimen can thus be scanned without the need for any pin-hole in front of the detector.

2.2. Structured Illumination microscopy (SIM)

3D scanning of an object with a focused laser beam is not the only possibility to obtain highly resolved 3D images by fluorescence microscopy. Instead, an extended pattern of excitation light may be used for imaging or scanning the object. According to the desired enhancement of structural information, various approaches of structured illumination microscopy have been described, such as standing wave field microscopy [15], spatially modulated illumination (SMI) [16] and patterned excitation/structured illumination microscopy (PEM/SIM) [17–19]. While SMI permits calculating images from well-defined planes of a sample in view of 3D imaging, the aim of SIM is to increase the spatial frequencies and thus the cutoff of the optical transfer function (OTF) within a microscope in order to improve the spatial resolution. In the linear (low illumination intensity) mode, SIM presently permits a lateral resolution around 100 nm and an axial resolution around 200 nm, using high numerical aperture objective lenses. From the point of optical theory, the achievable enhancement of resolution is about two times higher. When using the formulas mentioned above (plus an enhancement factor of 2) for a resolution estimate, a long working distance objective lens ($WD = 2$ cm, $A_N = 0.42$) would provide a lateral resolution around 360 nm and an axial resolution of about $2.2 \mu\text{m}$ ($\lambda = 500$ nm, $n = 1.515$). Important advantages of SIM for deep view imaging are low illumination intensity for *in vivo* imaging, application of any fluorescent dye used in conven-

tional fluorescence microscopy (including multicolour schemes) and combination with further techniques, e.g. LSFM or tomographic imaging ($\mu\text{-tom}$, s. below). If used in the nonlinear excitation mode [20], SIM allows even an ‘unlimited’ resolution enhancement. By using an innovative spot illumination pattern instead of grid lines, lattice SIM [21] overcomes some limitations of classic SIM regarding deep imaging with a higher contrast and robustness for image processing.

As an example for the application of SIM to improve contrast and resolution at large working distances ($WD \sim 1$ mm), Fig. 1 (left) shows a SIM image of an autofluorescent plant structure, using a low aperture objective lens ($A_N = 0.25$). In comparison with wide-field (WF) microscopy [Fig. 1 (right)], the smallest resolvable structures are reduced by SIM from about $10 \mu\text{m}$ to $2 \mu\text{m}$.

2.3. Light sheet fluorescence microscopy (LSFM)

One of the advantages of LSFM is that illumination of the samples commonly occurs with a low numerical aperture beam, i. e. mainly in the forward direction of the exciting laser beam. Due to the anisotropy of the scattering coefficient, light scattering also occurs preferentially in the forward direction, permitting higher penetration depths in comparison with high aperture illumination. Thus, penetration depths of $100\text{--}200 \mu\text{m}$ are obtained in non-cleared samples and more than $500 \mu\text{m}$ in cleared samples (Fig. 2). However, with increasing length of the light path, intensity and image quality decrease, and in some cases fluorescent stripes result from irregularities of optical scattering.

Light sheet fluorescent microscopy (LSFM) and SIM were recently combined in view of improving the lateral resolution as well as increasing the depth of imaging within a sample [23, 24], thus permitting penetrations depths up to $100 \mu\text{m}$.

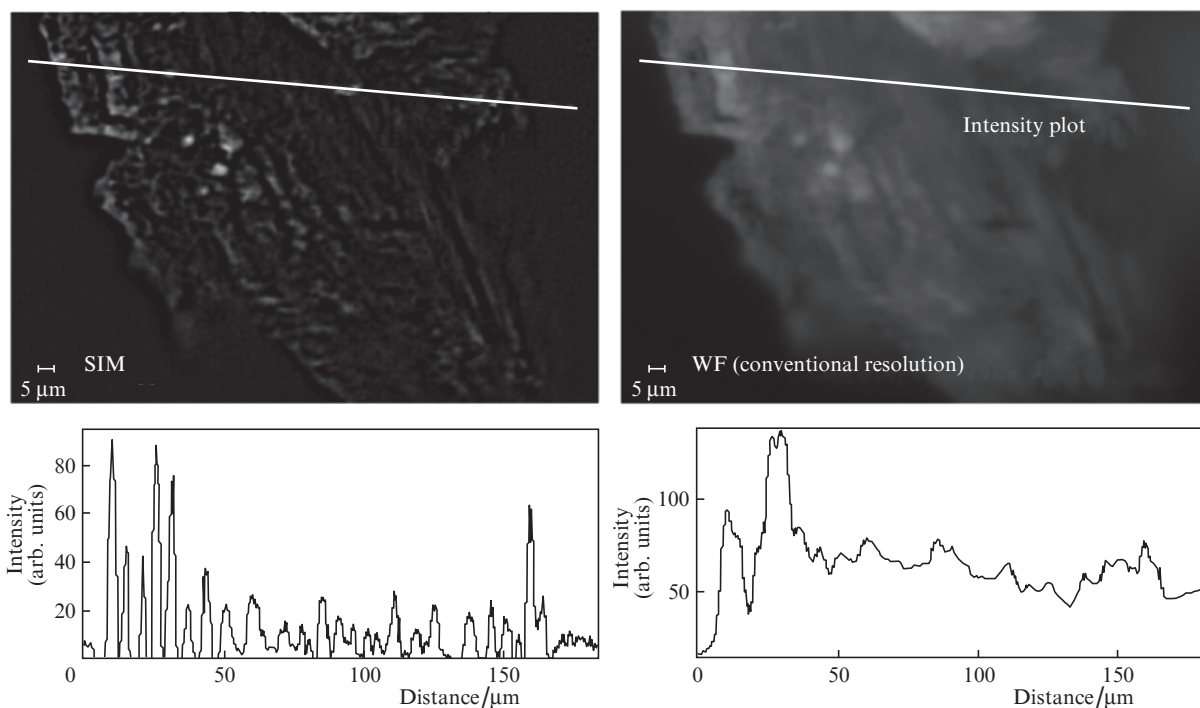


Figure 1. Enhancement of resolution and contrast by large working distance SIM; *Cedrus deodora*, autofluorescence including intensity profiles (below), $\lambda_{\text{ex}} = 671$ nm, $10\times/0.25$ microscope objective lens.

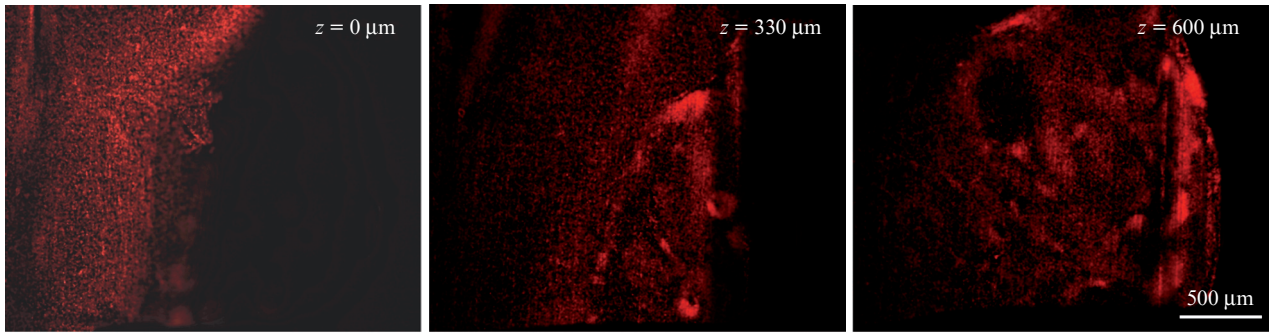


Figure 2. Light sheet fluorescence microscopy of a 1mm-thick mouse brain slice stained with Sytox Orange (DNA dye) and cleared with the CUBIC clearing method [22]. A z -stack of 61 images with 10 μm spacing was recorded. Representative images are shown from the stack at depths of 0, 330 and 600 μm ; the scale bar is 500 μm .

Presently the following concept is pursued: Structured illumination is created by letting the first diffraction orders of a spatial light modulator (SLM) interfere to generate a sinusoidal illumination pattern within a variable plane of the sample [25, 26]. A light sheet is generated in the same plane by the miniaturised module described in [5]. Therefore, the fluorescence intensity excited by structured light is enhanced in comparison with light scattered to other planes (which may be suppressed electronically). A more sophisticated approach is using light sheet modulated in intensity to which a continuous wave (cw) SIM signal is superimposed, as depicted in Fig. 3a. Detection occurs by a frequency modulated camera system at 1 MHz (FLIM camera, PCO AG, Kelheim, Germany; <https://www.pco.de/de/flim-kamera/pcoflim/>) originally designed for fluorescence lifetime imaging. Only within the selected light sheet the SIM signal is detected, whereas outside this light sheet the signal is discarded. Figure 3b shows an example for a monolayer of MCF-7 breast cancer cells incubated with the fluorescent dye CellTox (1 $\mu\text{L}/500 \mu\text{L}$) and illuminated by wide-field microscopy (left), SIM (middle) and SIM in combination with modulated LSFM (right). While SIM provides the expected increase in lateral and axial resolution, SIM + LSFM shows some clearer structures (in particu-

lar for the cells in the lower left and upper right part of the image) due to discrimination of scattered light. This appears important, since the contrast of the optical grating generated by SLM is rather low. Although Fig. 3b was recorded at a sample depth of (only) 12 μm , images at considerably larger depths may be generated for thicker samples, e.g. cell spheroids.

2.4. Axial tomography

A further option for deep view microscopy is optical tomography [27–30], where a sample is observed and measured from various sides. This requires specific rotatable sample holders, e.g. glass capillaries, into which specimens are embedded. Capillaries of cylindrical shape appear ideal for this purpose, and in some cases they can be inserted and optically coupled to a second, rectangular capillary [29], as depicted in Fig. 4. In addition to the larger observation volume upon rotation of the sample one can profit from the fact the most interesting parts of a specimen can be moved to the lateral plane, where resolution is always better than in axial direction. This results in a high and isotropic resolution in all three dimensions. Axial tomography has recently been applied from

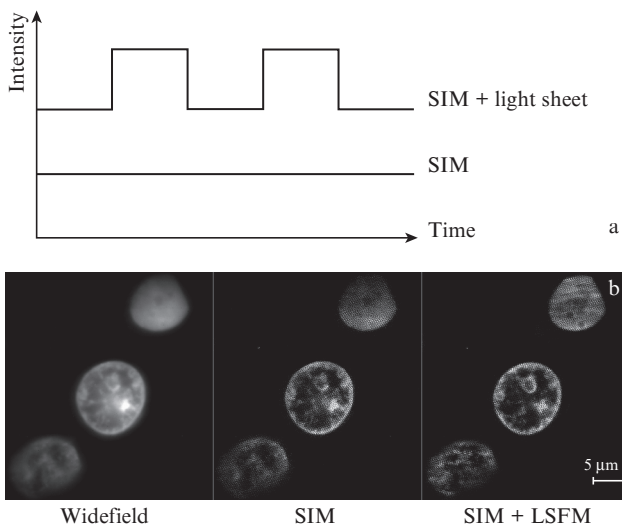


Figure 3. (a) Principle of combined (modulated light sheet and SIM) excitation; (b) fluorescence detection of MCF-7 breast cancer cells incubated with CellTox (1 $\mu\text{L}/500 \mu\text{L}$, $\lambda_{\text{ex}} = 488 \text{ nm}$ and $\lambda_{\text{d}} \geq 515 \text{ nm}$).

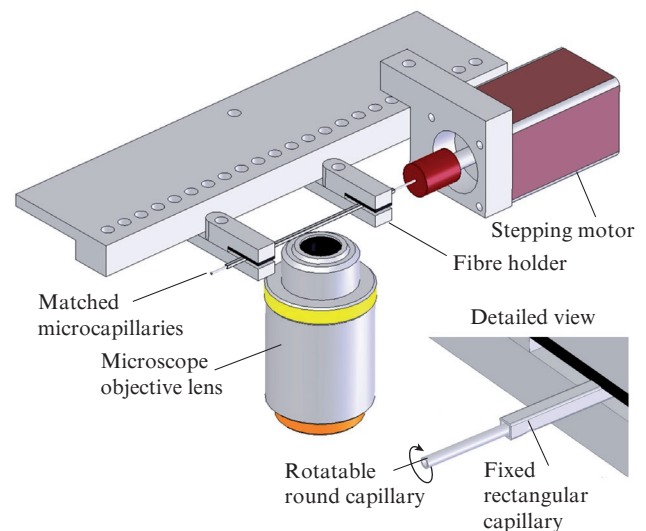


Figure 4. Sample holder for axial tomography using single or dual microcapillaries in an inverted microscope (reproduced from [29] with modifications).

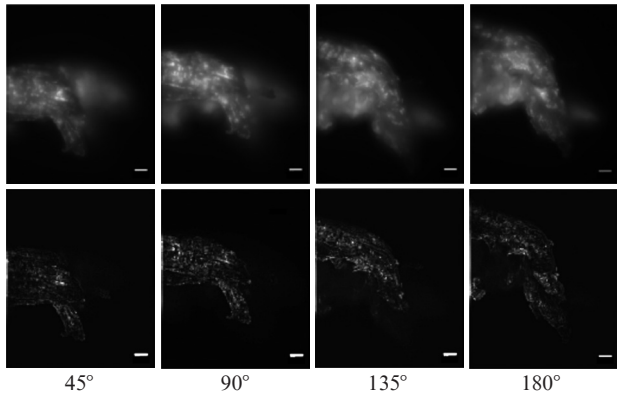


Figure 5. Combination of WF microscopy (upper row) and SIM (lower row) with axial tomography at large WDs ($A_N = 0.25$, $WD = 1$ mm); *Cedrus deodora*, $\lambda_{ex} = 671$ nm; the scale bar is $10 \mu\text{m}$.

microorganisms [29] down to single cells with improved sub-cellular resolution [30]. An example is again given in Fig. 5 for autofluorescence measurements of *Cedrus deodora* in combination with SIM.

2.5. Distributed aperture microscopy (DAM)

Since the axial resolution of both CLSM and SIM approaches deteriorates with the square of the A_N value, 3D resolution of a biological object (e. g. a cell) in the range of a few hundred

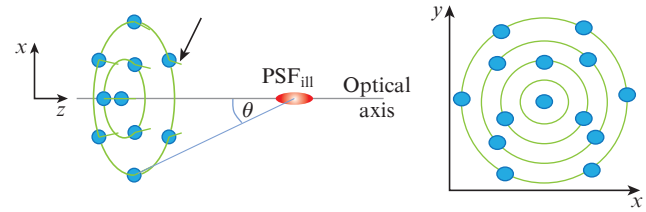


Figure 6. (Colour online) Schematic arrangement of light sources in DAM. Blue discs represent individual sources $S_1, S_2, \dots, S_K, \dots, S_N$ of coherent, collimated light at positions (x_K, y_K, z_K) with defined phase and polarisation relations emitting the light in defined directions (green, one indicated by a white arrow); the red 'spot' indicates the joint focal illumination distribution (i. e. the 'focal volume' or the 'observation volume of the illumination spot') produced by the constructive interference of the collimated waves. Altogether, the sources span a solid angle $\Omega = 2\pi(1 - \cos\vartheta)$, corresponding to the numerical aperture of a conventional objective lens with half opening angle ϑ . (Published in *Scientific Reports* under the Creative Commons Attribution License (CC-BY) [33] by Birk et al. [31].)

nm is possible with high A_N only, i. e. at relatively low working distances. For example, for 3D resolution $(x, y, z) \leq 300$ nm, SIM would require a numerical aperture of about 1.1, corresponding to a WD in the $200 \mu\text{m}$ range. This excludes larger objects, such as cell spheroids, embryos, or tissues to be imaged at such a high 3D resolution.

These limits may be eliminated, however, using an illumination device with multiple collimated laser beams (distributed

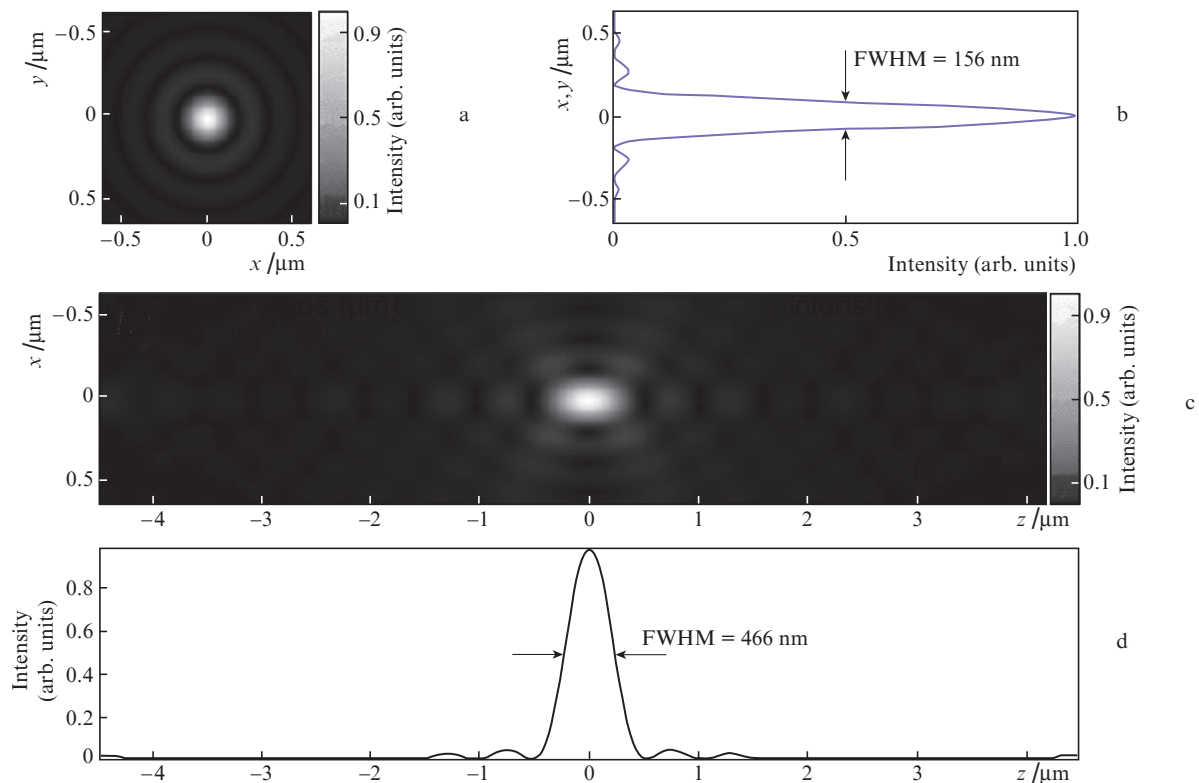


Figure 7. Focal spot for sources covering a solid angle of $\Omega = 1.25\pi$. Intensity distribution calculated for 6 580 sources distributed over $\Omega = 2\pi(1 - \cos\vartheta) = 1.25\pi$ (this corresponds to an objective lens with $A_N = 1.4$). In this calculation, the refractive index at the position of the focus is given by $n = 1.518$. (a) Lateral distribution of the focal intensity $F(x, y)$; (b) profile across the lateral focus intensity distribution along the x or y axis; (c) x - z section through the focus intensity distribution; (d) the corresponding axial profile $F_{x=y=0}(z)$. In principle, the light sources may be positioned at arbitrary large distances from the focal region. (Published in *Scientific Reports* under the Creative Commons Attribution License (CC-BY) [33] by Birk et al [31].)

aperture illumination, DAI) directed constructively to a given object region (distributed aperture microscopy, DAM [31]). In addition to point scanning modes (including stimulated emission depletion (STED) microscopy [32]), DAM can also be applied to allow pattern-based scanning modes like SIM) and LSM, optical projection microscopy, or axial tomography. A decisive additional advantage of DAM in this respect is the possibility to program the DAI in such a way that the switching between different imaging modes can be done very fast.

Figure 6 shows schematically the general arrangement to realise the multi-beam illumination concept of DAI: A number of point sources ($i = 1, 2, 3, \dots, N$) emitting collimated beams are arranged at defined positions $r_i = (x_i, y_i, z_i)$ around the optical axis of the focusing DAM system. The following coordinate system is used: The geometrical center at which all sources are directed defines the origin $O = (0, 0, 0)$ (red). The optical axis (z) is defined by the origin and the geometrical centre of all sources. The spatial arrangement (i. e. the sites of the light sources) can be modified, covering a certain solid angle (Ω) around the origin. The sources emit light in form of collimated beams, directed towards the origin. The path length from all sources to the origin is equal (modulo 2π), resulting in constructive interference such that the field in the origin is maximised. Thus, the intensity distribution around the origin can be considered as a ‘focal spot’. In this configuration, the plane perpendicular to the optical axis through the origin can be termed the focal plane, and the illumination

intensity distribution across this plane is thus termed the lateral focus intensity distribution. In contrast to objective lens based illumination devices, the spatial location, the power, phase and polarisation states of each of the beams can be controlled individually.

Figure 7 shows the result of detailed numerical calculations approximating the focus of a high aperture objective lens by a distributed array of such phase matched laser beams. Using an appropriate array of multiple collimated laser beams, an illumination focus with a full-width-at-half-maximum (FWHM) spot around 160 nm in all directions can be produced ($\lambda = 488$ nm; $n = 1.518$) in a homogeneous, transparent medium.

Since each of the coherent light beams is collimated, the distance of the sources is in principle arbitrary, i. e. this distance can be varied within large limits (up to several cm or more, e. g. 5 cm or even larger); this, however, is equivalent to the possibility to realise a joint ‘focal spot’ for scanning based imaging. The joint ‘focal spot’ can be made substantially smaller than possible with low aperture objective lenses appropriate to realise the same large working distance; hence, an enhanced resolution will be obtained compared with a lens based system at the same large working distance. Similar to the increased resolution obtained with multiple illumination light sources, multiple object ‘sources’ can be used to obtain an increased resolution [34].

The concept of DAI can also be implemented into various super-resolution microscopy approaches (for reviews see

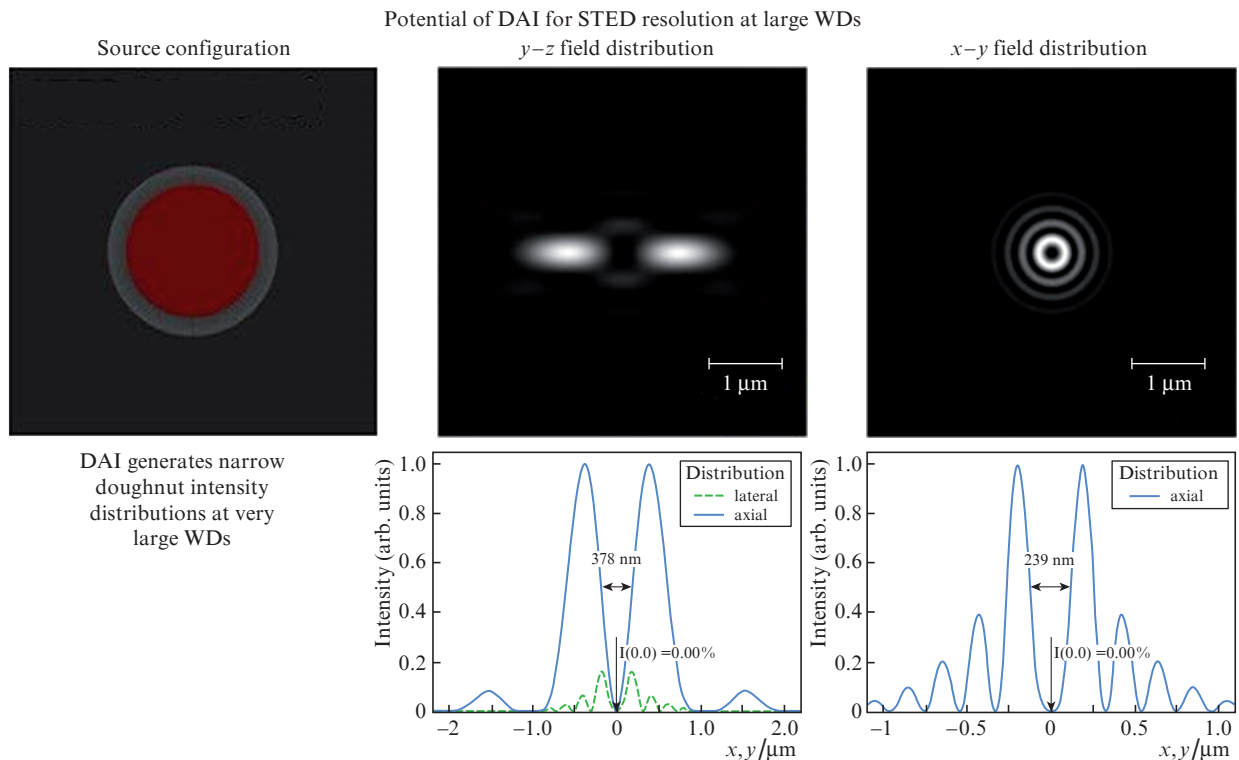


Figure 8. Implementation of STED/MINFLUX mode. Left: z projection of the arrangement of $N = 6576$ coherent light sources (e. g. glass fibres with a low numerical aperture) directed towards the origin. Sources are distributed within a solid angle of $\Omega = 2\pi(1 - \cos\theta) = 1.25\pi$ (this corresponds to an objective lens with $N_A = 1.4$). Centre: $y-z$ section across the intensity distribution around the origin. The given STED beam width (left: 378 nm, right: 293 nm) refers to the FWHMs of the respective minima ($z; x, y$). Right: $x-y$ section across the intensity distribution around the origin. For STED-type illumination, half of the sources in the centre were phase-delayed by π . In principle, the STED producing light sources may be positioned at arbitrary large distances from the focal region. Instead of using the doughnut structure at high illumination intensities for STED, it may be used in the low illumination ‘MINFLUX’ mode for enhancing the optical resolution down to the nm range [38]. (Published in *Scientific Reports* under the Creative Commons Attribution License (CC-BY) [33] by Birk et al [31].)

[35, 36]. For example, the DAI patterns can be generated in such a way that in addition to a diffraction limited focused beam, the generation of a depletion focus similar to that implemented in a STED microscope is possible; or an appropriately structured light pattern can be produced to allow for a localisation microscopy based ‘MINFLUX’ scheme [37]. The results of such numerical calculations are depicted in Fig. 8. If such a DAI based STED intensity distribution is applied to a previously excited ensemble of fluorophores, the concept of fluorescence depletion in the vicinity of the origin can be realised at arbitrarily large working distances, without requiring the STED illumination intensities to be significantly higher than usually applied e.g. in commercial STED systems. In this way, a STED resolution down to few tens of nm can be realised at working distances up to the multi-centimetre range; in the MINFLUX mode, a resolution enhancement down to the 1 nm range appears to become feasible at similarly large working distances.

3. Discussion

Examination of deeper areas within a specimen is a main challenge for microscopy of 3D cell or tissue samples. Hereby, selection of specific layers and suppression of other parts of the sample, e.g. by confocal laser scanning microscopy or light sheet microscopy, is cogent. Focusing to larger depths within a sample requires long working distances at a low or moderate aperture of objective lenses. This limits the resolution and increases the depth of focus, as reported above. Super-resolution techniques, e.g. by structured illumination, however, can still be applied.

Usually the penetration depth of light in cell or tissue samples is limited due to high scattering and moderate absorption coefficients, which can be reduced by optical clearing techniques in biopsies or fixed specimens (see e.g. Fig. 2), but not in living cells or tissues. However, both absorption and scattering coefficients decrease at longer wavelengths. Therefore, red or near-IR absorbing dyes [39, 40] as well as multiphoton excitation techniques are used increasingly.

Further applications include phase modulated detection (Fig. 3) or up-conversion techniques to reduce the influence of light scattering. In the latter case [41], up-conversion of an IR ultrashort laser pulse (‘gate pulse’) and a second pulse (‘signal’) passing through the sample occurs within a nonlinear crystal. Since the second pulse is broadened due to light scattering, a sum frequency is generated only when the pulses overlap temporally, i.e. at the leading edge of the signal representing the least scattered (‘ballistic’) photons. This method is used for multiple view acquisition in a technique called time-gated optical projection tomography. In addition, self-interference 3D techniques based on super-localisation microscopy are used for deep tissue imaging [42].

At larger depths within a sample geometric as well as chromatic aberrations play an increasing role. These aberrations can at least in part be corrected by adaptive optics, e.g. deformable mirrors or spatial light modulators [43]. Therefore, adaptive optics as well advanced reconstruction algorithms (see e.g. [44]) may increase image quality in deeper layers of a specimen.

Distributed aperture microscopy offers completely new possibilities for 3D/deep view imaging. Presently, these applications are highly restricted due to the very small working distance in high aperture ‘conventional’ super-resolution microscopy. However, DAM may permit producing a very small

focal diameter for point-by-point-scanning of the object at arbitrarily large working distances and to detect efficiently the generated signal (e.g. fluorescence or scattering). Furthermore, it should be possible to perform STED/MINFLUX at a substantially larger working distance than upon use of conventional objective lens based systems. In all those cases, a large working distance combined with high resolution is required. Biomedical examples are 3D microscopy of small model organisms, of cell spheroids in developmental biology, cancer research and pharmacology, neuronal ‘microbrains’/brain tissues in neurobiology, or entire organs, made suitably transparent by the tissue clearing method.

The problem of extinction of light in inhomogeneities is primarily a problem of variable optical path lengths dependent on the starting point of the light quantum. In principle, DAM allows independent adjustment of the phase relationships of the individual coherent beams. This might permit correction of the local refraction index inhomogeneities of the sample.

Acknowledgements. The authors thank Prof. Heiko Luhmann and Dr. Anne Sinning, Institute of Physiology, as well as Prof. Beat Lutz, Institute of Physiological Chemistry, University Medical Center Mainz, for their cooperation. A phase resolving FLIM camera was provided by PCO AG, Kelheim, Germany.

References

1. Pawley J. *Handbook of Biological Confocal Microscopy* (Boston, MA, USA: Springer, 1990); doi.org/10.1007/978-0-387-45524-2.
2. Webb R.H. *Rep. Progr. Phys.*, **59**, 427 (1996).
3. Pampaloni F., Chang B.-J., Stelzer E.H.K. *Cell Tissue Res.*, **362** (1), 265 (2015); doi.org/10.1007/s00441-015-2144-5.
4. Santi P.A. *J. Histochem. Cytochem.*, **59** (2), 129 (2011); doi.org/10.1369/0022155410394857.
5. Bruns T., Bauer M., Bruns S., Meyer H., Kubin D., Schneckenburger H. *J. Microsc.*, **264** (3), 261 (2016); doi.org/10.1111/jmi.12439.
6. Staier F. et al. *Rev. Sci. Instrum.*, **82** (9), 093701 (2011); doi: 10.1063/1.3632115.
7. Sdobnov A.Yu., Lademann J., Darvin M.E., Tuchin V.V. *Biochemistry (Moscow)*, **84**, 144 (2019) [*Usp. Biol. Khim.*, **59**, 295 (2019)]; doi: 10.1134/S0006297919140098.
8. Feng W., Zhang C., Yu T., Zhu D. *Biomed. Opt. Express.*, **10** (6), 2996 (2019); doi: 10.1364/BOE.10.002996.
9. Costa E.C., Silva D.N., Moreira A.F., Correia I.J. *Biotechnol Bioeng.*, in press (2019); doi: 10.1002/bit.27105.
10. Huff J. *Nature Meth.*, **12** (12), (2015); doi: 10.1038/nmeth.f.388.
11. Müller C.B., Enderlein J. *Phys. Rev. Lett.*, **104** (19), 198101 (2010); doi.org/10.1103/PhysRevLett.104.1981.
12. de Luca G.M.R., Breedijk R.M.P., Brandt R.A.J., Zeelenberg C.H.C., de Jong B.E., Timmermans W., Nahidi Azar L., Hoebe R.A., Stallinga S., Manders E.M.M. *Biomed. Opt. Express*, **4** (11), 2644 (2013); doi.org/10.1364/BOE.4.002644.
13. Denk W., Strickler J.H., Webb W.W. *Science*, **248** (4951), 73 (1990); doi: 10.1126/science.2321027.
14. König K. *J. Microsc.*, **200** (Pt 2), 83 (2000); doi: 10.1046/j.1365-2818.2000.00738.x.
15. Bailey B., Farkas D.L., Taylor D.L., Lanni F. *Nature*, **366** (6450), 44 (1993).
16. Baddeley D., Batram C., Weiland Y., Cremer C., Birk U.J. *Nat. Protoc.*, **2** (10), 2640 (2007); doi: 10.1038/nprot.2007.399.
17. Heintzmann R., Cremer C. *Proc. SPIE*, **3568** (1999); doi: 10.1117/12.336833.
18. Gustafsson M.G.L. *Curr. Opin. Struct. Biol.*, **9**, 627 (1999); doi: 10.1016/s0959-440x(99)00016-0.
19. Gustafsson M.G.L. *J. Microsc.*, **198**, 82 (2000); doi: 10.1046/j.1365-2818.2000.00710.x.

20. Heintzmann R., Jovin T., Cremer C. *J. Opt. Soc. Am. A*, **19**, 1599 (2002); doi: 10.1364/JOSAA.19.001599.
21. Betzig E. *Opt. Express*, **13** (8), 3021 (2005); doi: 10.1364/OPEX.13.003021.
22. Susaki E.A., Kazuki T., Perrin D., Yukinaga H., Kuno A., Ueda H.R. *Nature Protocols*, **10** (11), 1709 (2015); doi: 10.1038/nprot.2015.085.
23. Chang B.J., Perez Meza V.D., Stelzer E.H.K. *Proc. Natl. Acad. Sci. USA*, **114** (19), 4869 (2017); doi: 10.1073/pnas.1609278114.
24. Chen B.C., Legant W.R., Wang K., Shao L., Milkie D.E., Davidson M.W., Janetopoulos C., Wu X.S., Hammer J.A., Liu Z. et al. *Science*, **346** (6208), 1257998 (2014); doi: 10.1126/science.1257998.
25. Förster R., Lu-Walther H.-W., Jost A., Kielhorn M., Wicker K., Heintzmann R. *Opt. Express*, **22** (17), 20663 (2014); doi: 10.1364/OE.22.020663.
26. Richter V., Piper M., Wagner M., Schneckenburger H. *Appl. Sci.*, **9** (6), 1188 (2019); doi: 10.3390/app9061188.
27. Bradl J., Rinke B., Schneider B., Edelmann P., Krieger H., Hausmann M., Cremer C. *Microscopy & Analysis*, **11**, 9 (1996).
28. Heintzmann R., Cremer C. *J. Microsc.*, **206** (1), 7 (2002).
29. Bruns T., Schickinger S., Schneckenburger H. *J. Microsc.*, **260** (1) 30 (2015); doi: 10.1111/jmi.12263.
30. Richter V., Bruns S., Bruns T., Weber P., Wagner M., Cremer C., Schneckenburger H. *J. Biomed. Opt.*, **22** (9) 91505 (2017); doi: 10.1117/1.JBO.22.9.091505.
31. Birk U., von Hase J., Cremer C. *Sci. Reports*, **7** (1), 3685 (2017); doi: 10.1038/s41598-017-03743-4.
32. Hell S.W., Wichmann J. *Opt. Lett.*, **19** (11), 780 (1994); doi: 10.1364/OL.19.000780. doi.org/10.1364/OL.19.000780.
33. Creative Commons – Attribution International – CC BY 4.0; <https://creativecommons.org/licenses/by/4.0/>.
34. Baddeley D. et al. *J. Microscopy*, **237** (1), 70 (2010); doi: 10.1111/j.1365-2818.2009.03304.x.
35. Cremer C., Masters B.R. *Europ. Phys. J. H*, **38** (3), 281 (2013), doi: 10.1140/epjh/e2012-20060-1.
36. Cremer C., Szczurek A., Schock F., Gourram A., Birk U. *Methods*, **123**, 11 (2017), doi: 10.1016/j.ymeth.2017.03.019.
37. Balzarotti F. et al. *Science*, **355** (6325), 606 (2017); doi: 10.1126/science.aak9913.
38. Best G. et al. US Patent 9, 874 , 737 B2, filed May 7, 2014 (granted Jan 23, 2018).
39. Ring H.C., Israelsen N.M., Bang O., Haedersdal M., Mogensen M. *J. Biophoton.*, **12** (6), e201800462 (2019); doi: 10.1002/jbio.201800462.
40. Grzybowski M. et al. *Angew. Chem. Int.*, **57** (32), 10137 (2018); doi: 10.1002/anie.201804731.
41. Fieramonti L., Bassi A., Foglia E.A., Pistocchi A., D’Andrea C., Valentini G., Cubeddu R., De Silvestri S., Cerullo G., Cotelli F. *PLoS ONE*, **7** (11), e50744 (2012); doi: 10.1371/journal.pone.0050744.
42. Bon P., Linares-Loyez J., Feyeux M., Alessandri K., Lounis B., Nassoy P., Cagnet L. *Nat Meth.*, **15** (6), 449 (2018); doi: 10.1038/s41592-018-0005-3
43. Booth M., Andrade D., Burke D., 1, Patton B., Zurauskas M. *Microscopy*, **64** (4), 251 (2015); doi: 10.1093/jmicro/dfv033.
44. Birk U. *Genes*, **10** (7), 493 (2019); doi: 10.3390/genes10070493.